Optical and Crystal Structure Properties of ZnO Nanoparticle Synthesized through Biosynthesis Method for Photocatalysis Application

Sri Wahyu Suciyati[1,2*], Posman Manurung[2], Junaidi Junaidi[2], and Rudy Situmeang[3]**

[1]*Doctoral Program of Mathematics and Natural Sciences, University of Lampung, Jl. Prof. Dr. Ir. Sumantri Brojonegoro No. 1, Bandar Lampung 35145, Indonesia*

[2]*Department of Physics, Faculty of Mathematics and Natural Sciences, University of Lampung, Jl. Prof. Dr. Ir. Sumantri Brojonegoro No. 1, Bandar Lampung 35145, Indonesia*

[3]*Department of Chemistry, Faculty of Mathematics and Natural Sciences, University of Lampung, Jl. Prof. Dr. Ir. Sumantri Brojonegoro No. 1, Bandar Lampung 35145, Indonesia*

* ***Corresponding author:***

email: sri.wahyu@fmipa.unila.ac.id; posman.manurung@fmipa.unila.ac.id***

Received: May 26, 2023
Accepted: November 23, 2023

DOI: 10.22146/ijc.84796

Abstract: *In this study, zinc oxide nanoparticles (ZnO NPs) were synthesized from zinc nitrate hexahydrate precursor and mango leaf extract (MLE). The purpose of this research was to investigate the crystal structure and optical properties exhibited by ZnO NPs for photocatalytic applications. ZnO NPs produced from various concentrations of sodium hydroxide (NaOH) and the addition of MLE during the synthesis stage demonstrated intriguing physical structure and optical properties. XRD characterization results revealed the attainment of a pure ZnO phase with a high crystallinity degree in all samples. Biosynthesis with MLE unveiled minor peaks corresponding to the cellulose phase. The achieved crystallite size ranged from 15–28 nm. The FTIR patterns detected in the wavenumber range of 600–4000 cm^{-1} indicated successful crystallization of all ZnO NPs samples. The band gap energy for each sample (ZnO-A to ZnO-E) is indicated to be in the range of 3.25, 3.25, 3.26, 3.31, and 3.17 eV, as demonstrated by the Tauc relation. The effect of MB degradation by the ZnO-E photocatalyst is revealed by the photodegradation of 96.46%.*

Keywords: *ZnO NPs; crystal structure; biosynthesis; functional group; band gap energy*

■ INTRODUCTION

Some metal oxide materials are being produced as nanomaterials for various industrial applications, including catalysis, sensors, environmental remediation, medicine, food, and cosmetics [1-6]. From the point of view of photocatalytic applications, zinc oxide (ZnO) and titanium oxide (TiO_2), are synthesized as nanoparticles [7-8] due to their increased ability as photocatalysis degradation. However, according to several studies [7-10], ZnO nanoparticles (ZnO NPs) are more active than TiO_2 in killing bacteria, so commercially, they have become an essential material to be developed. Apart from being an antibacterial, several publications also report using ZnO NPs as an adsorbent or photocatalyst to remove dyes [11-13].

As a metal oxide, ZnO is a semiconductor (II-VI), which has properties such as good transparency, high electron mobility, wide band gap energy, and substantial room temperature luminescence, so it is widely developed as an environmentally friendly photocatalyst, medical, and environmental remediation [14-17]. This photocatalyst shows the appropriate energy potential for oxidation and reduction processes on the semiconductor surface [17]. Like the bulk material, ZnO NPs have a hexagonal wurtzite crystal structure with a band gap energy of 3.32 to 3.77 eV. This structure has high optical transparency in the visible light spectrum. The wurtzite system is very stable at room temperature, so it has been widely studied for environmental improvement and the production of photovoltaic energy [18-20]. The exciton binding energy of ZnO NPs is

about 60 meV, allowing excitonic transitions at room temperature and high radiation recombination efficiency for spontaneous emission. Furthermore, ZnO at the nanoscale level renders it a promising material for use in high-performance devices in nanotechnology and is easily synthesized [21-24].

Various methods have been reported to synthesize ZnO nanoparticles, but hydrothermal and precipitation processes have several advantages, including low processing temperature, low cost, and environmental friendliness. Treatment, time, and methods used during synthesizing ZnO NPs affect the results obtained, so studying one of these parameters will provide interesting information.

Treatments utilizing plants for the synthesis of ZnO NPs have been widely conducted, as evidenced by various studies on plants, such as *Moringa oleifera* [15], *Mangifera indica* [16-17], *Bergera koenigii* [25], *Rosmarinus officinalis* [26], *Pandanus odorifer* [27], *Polygala tenuifolia* [28], *Hibiscus sabdariffa* [29], *Sambucus ebulus* [30], and *Laurus nobilis* [31]. The superiority of plants is revealed due to their biocompatibility, environmental friendliness, and cost-effectiveness in producing ZnO NPs.

Mango (*M. indica*) is found in almost all regions of Indonesia, making it an abundant source of raw materials for the biosynthesis of ZnO NPs. The utilization of abundant phytochemical content such as flavonoids, saponins, carotenoids, alkaloids, and phenolics in plants supports their use as reducing agents and capping agents in the biosynthesis of ZnO NPs. The biosynthesis of ZnO NPs has been undertaken using mango leaves [16,32] and mango seeds [33], both of which are rich in phenolic acids, xanthones, benzophenones, tannins, terpenoids, and flavonoids [34]. While ZnO NPs synthesized using mango leaf extract [26,32] and mango seeds [33] are recognized for medical applications, their use for photocatalysis purposes has not been reported to date. Mango leaves were chosen as the raw material in this research because they are easier to obtain than mango seeds.

In this research, ZnO NPs will be synthesized through two treatments: first, without the addition of mango (*M. indica*) leaf extract (MLE), and second, by adding MLE (biosynthesis) into the solution of zinc nitrate and sodium hydroxide (NaOH). The biosynthesis of ZnO NPs will lead to an enhancement in the dispersion properties of ZnO in the solution, resulting in uniform particle sizes and the mitigation of aggregation issues in ZnO NPs, as demonstrated by Wijesinghe et al. [35]. The synthesis method employed is hydrothermal and precipitation; not only is this method simple and characterized by low energy consumption, but it also operates at relatively mild temperature and pressure conditions during the synthesis process. Additionally, the hydrothermal method offers the advantage of producing ZnO NP powder with a high level of crystallinity at low temperatures [18,36-38], significantly expediting synthesis kinetics [19]. In this research, the mass of NaOH will be varied. MLE will be added as a precipitating agent and capping agent to assess their respective effects on the structure and morphology of the ZnO NPs.

Furthermore, the impact of NaOH and MLE solution on the physical structure, surface morphology, chemical composition, and optical properties of ZnO NPs was analyzed through X-ray diffraction (XRD), scanning electron microscopy (SEM), transmission electron microscopy (TEM), Fourier transform infrared (FTIR), and ultraviolet-visible diffuse reflectance spectroscopy (UV-vis-DRS). Information obtained from biosynthetically synthesized ZnO NPs can be a reference for developing ZnO NPs as a photocatalyst material.

■ EXPERIMENTAL SECTION

Materials

The materials used in this study were zinc nitrate hexahydrate ($Zn(NO_3)_2{\cdot}6H_2O$, 95%, Merck), NaOH (75%, Merck), deionized water, ethanol (C_2H_5OH, 97%, Merck), and mango leaf. All materials were used without further purification.

Instrumentation

The crystalline structure of ZnO NPs was analyzed by XRD using a Panalytical XPert Pro diffractometer operating at 30 kV and 40 mA using CuKα radiation

(λ = 1.54060 Å) with a step size of 0.02°. Data was recorded in the range of 2θ 10–80° with rotation goniometry. The morphology of the samples was analyzed using SEM from Zeiss EVO MA 10 and TEM from FEI-Tecnai G2 20 S-Twin. Functional groups were observed using the FTIR from Agilent/FTIR CARY 630. The UV-vis absorbance spectra determined the optical band gap using CARY 100 Spectrophotometer Shimadzu.

Procedure

Preparation of MLE

Mango leaves were washed under running water to remove dust particles, and then 5 g of mango leaves were cut into pieces and placed in a beaker glass containing deionized water (100 mL). The leaves were soaked for 5 min and then placed in a water bath at 70°C for 30 min. The leaf solution was allowed to cool and filtered using Whatman filter paper number-1 to obtain MLE for further use.

Preparation and chemical synthesis ZnO NPs

ZnO nanoparticle powder was obtained via the hydrothermal method. First, 2.97 g of $Zn(NO_3)_2{\cdot}6H_2O$ was dissolved in 2 mL of deionized water. Second, NaOH solutions were prepared by dissolving various mass values (1, 2, 3, 4 g) in 20 mL of deionized water. Third, the $Zn(NO_3)_2{\cdot}6H_2O$ solution with a concentration of 5 mol/L was dripped with NaOH solution, each with a concentration of 1.25, 2.50, 3.75, and 5.00 mol/L, so 4 samples were obtained. This mixture was stirred for 3 h, after which the solution was placed into an autoclave and heated at 100 °C for 8 h. Next, the autoclave was allowed to cool for 24 h; then, the solution was transferred to tubes for centrifugation. This process uses ethanol and deionized water alternately to obtain a filtrate, ready to be dried at 100 °C for 3 h, and then the samples were ground using an agate mortar to get ZnO NPs powder. The samples obtained are called ZnO-A (1.25 mol/L of NaOH), ZnO-B (2.50 mol/L of NaOH), ZnO-C (3.75 mol/L of NaOH), and ZnO-D (5.00 mol/L of NaOH).

Preparation and biosynthesis of ZnO NPs

ZnO NPs were synthesized using the precipitation method. In this procedure, 0.2 mol/L $Zn(NO_3)_2{\cdot}6H_2O$ was dissolved in 50 mL deionized water and subjected to a magnetic stirrer for 1. Next, 20 mL of 0.1 mol/L solution of NaOH was added slowly to the $Zn(NO_3)_2{\cdot}6H_2O$ solution using a pipette, and the mixture was stirred with a magnetic stirrer for an additional hour. Next, 25 mL of MLE solution was added, and the mixture was mixed with a magnetic stirrer for 3 h. During the first hour of incubation, the color of the mixture gradually changed to yellow, confirming the formation of ZnO NPs. The resulting precipitate was filtered and washed alternately with deionized water and ethanol. Next, the filtrate was dried at 80 °C for 2 h. After drying, the sample was ground using an agate mortar until a fine white powder, namely ZnO NPs (ZnO-E), was obtained.

Particle size was calculated from XRD data using the Scherrer Eq. (1);

$$D = \frac{0.9\lambda}{B\cos\theta} \quad (1)$$

where λ = X-ray wavelength (Å), B = full width at half maximum (FWHM)(rad), and θ = scattering angle (°). The lattice strain parameter (ε) can be calculated using XRD pattern data using Eq. (2);

$$\varepsilon = \frac{B}{4\tan\theta} \quad (2)$$

which is a modified form of the Williamson-Hall formula [39-40]. Furthermore, the dislocation density, δ, is the length of the dislocation lines to the unit volume of the crystal, which can be calculated from Eq. (3);

$$\delta = \frac{1}{D^2} \quad (3)$$

where D is particle size.

The estimated band gap value can be obtained by applying the Tauc relationship [41], which is expressed by the Eq. (4);

$$(\alpha h\nu)^{1/n} = A\left(h\nu - E_g\right) \quad (4)$$

where h, A, ν, E_g, α, and n are Plank's constant = 6.6×10^{-34} J s, proportionality constant (J), frequency (Hz), band gap energy (eV), and absorption coefficient, and value of the type of transition in the semiconductor material, respectively. For direct and indirect transitions, the n values are ½ and 2. Because ZnO is a direct transition semiconductor, the n value is ½.

Photocatalyst activity is interpreted through analysis of photocatalytic data, especially on the reaction

kinetics calculated using the pseudo-first-order kinetic (Eq. (5)). The efficiency of the degradation of the methylene blue (MB) is calculated by Eq. (6) [28].

$$\ln\frac{C}{C_0} = -kt \quad (5)$$

$$\%\ \text{Degradation} = \left(\frac{A_0 - A}{A_0}\right) \times 100\% \quad (6)$$

Photocatalytic application of ZnO-E

ZnO-E sample was used to degrade MB with a concentration of 10 ppm. MB (100 mL) was added with 3.5 g of ZnO-E photocatalyst and irradiated with sunlight for 90 min with an interval of 30 min. The photocatalytic activity was analyzed using a Shimadzu CARY 100 Spectrophotometer with a 200–800 nm wavelength range. Exposure time is approximately 11.00 to 13.00 in July 2023.

■ RESULTS AND DISCUSSION

XRD Analysis

Qualitative analysis

Fig. 1 shows the XRD diffractogram of ZnO NPs synthesis grown at 100 °C for 8 h and the XRD pattern of ZnO NPs biosynthesis for 5 h. XRD patterns showed crystalline structure and broadening of the characteristic line of the ZnO nanoparticles. A typical XRD pattern for a hexagonal structure shows the three most robust lines at a 2θ value of 31.8–32.06° [100], 34.4–34.76° [002], and 36.27–36.56° [101]. The result of the qualitative analysis showed that the diffraction peaks match the zinc oxide phase of Powder Diffraction File card database No. 01-089-0510 [42].

Fig. 1 shows a shift in the 2θ diffraction peaks, which is associated with an increase in the mass of NaOH. The diffraction peak's widening represents the material's crystallite size becoming smaller. The varying intensity and widening of the peaks represent the rearrangement of the crystal planes according to the synthesis conditions, which are influenced by the mass of NaOH [43-45]. In general, the 2θ and FWHM angle shifts in samples (ZnO-A to ZnO-D) are due to the influence of the addition of NaOH concentration, where the pH value of each solution is 11, 12, 13, and 14, respectively. The effect of pH on crystallite size, according to Nath et al. [46], has

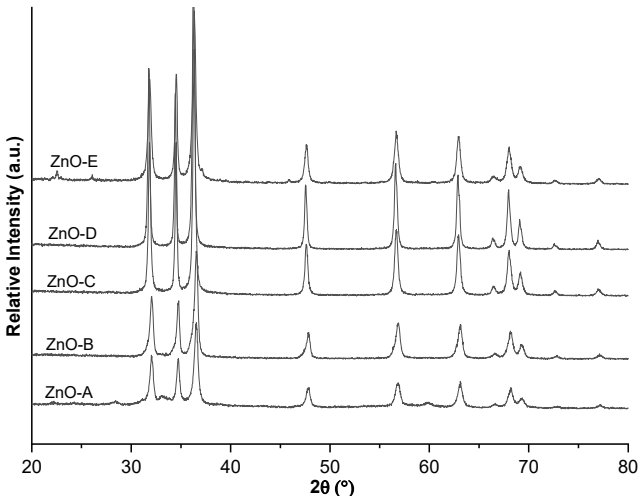

Fig 1. XRD diffractogram of ZnO NPs in various concentrations of NaOH grown at 100 °C for 8 h (ZnO-A to ZnO-D) and 5 h (ZnO-E).

increased the crystallite size. This explains that during the synthesis process, there is an increase in the reaction rate due to the increase in the concentration of NaOH, so more $Zn(OH)_2$ nuclei are formed, and there is more chance for crystal growth. In ZnO-E, besides NaOH affecting the growth of ZnO NPs, MLE also reduced and stabilized the sample.

Table 1 shows the difference between the *d* spacing of data and the *d* spacing of the database is less than 0.011 Å, which indicates good matching between theory and data. FWHM becomes smaller when the NaOH solution becomes more alkaline, and it is directly related to the crystallite size. The sample's crystallite size increases with the increase in the concentration of NaOH. It also means that increasing the concentration of NaOH as a precipitating agent impacts reducing the width of the diffraction peaks. At the same time, it was revealed that the crystals grew very well due to the growing environment, which was increasingly alkaline [47].

pH is an essential factor that reduces metal ions by changing the electrical charge of molecules, thereby changing the ability to mitigate and grow nanoparticles. An increasingly alkaline solution will accelerate the growth rate in the solution due to the high concentration of OH^-. The abundant amount of OH^- ions causes a strong attraction between Zn^{2+} ions and OH^- ions, thereby

Table 1. Crystallites size of all samples. Each sample represents the concentration of NaOH used in the synthesis. ZnO-A = 1.25 mol/L, ZnO-B = 2.50 mol/L, ZnO-C = 3.75 mol/L, ZnO-D = 5.00 mol/L, ZnO-E = 0.25 mol/L (biosynthesis)

Samples	2θ (°)	B (FWHM) (°)	*d* spacing, d_{XRD} (Å)	*d* spacing, d_{PDF} (Å)	$\|\Delta d$ (Å)$\|$	Crystallites size (nm)
ZnO-A	36.56	0.549	2.4581	2.46903	0.01093	15.2
ZnO-B	36.54	0.499	2.4587	2.45753	0.00117	16.8
ZnO-C	36.32	0.349	2.4724	2.47513	0.00273	23.9
ZnO-D	36.27	0.296	2.4756	2.47608	0.00048	28.2
ZnO-E	36.34	0.454	2.4726	2.47523	0.00263	18.4

increasing the formation of crystallization and forming smaller ZnO NPs grain sizes [48]. In ZnO-E, apart from the alkaline effect, the presence of phytochemicals in the MLE also played an important role, not only as a reducing agent but also as a control of the growth of ZnO NP crystallites. The phytochemicals in the leaf extract significantly prevent the crystallization of ZnO by interacting with free Zn^{2+} ions during the reduction process [49]. This means that the process of crystallization of ZnO is controlled during the reduction process.

The widening of the XRD diffraction peaks indicates a deviation from the perfection of the crystallinity of ZnO NPs so that the lattice strain is considered a measure of the lattice distribution due to crystal imperfections (lattice dislocations). The lattice strain values for each ZnO NPs sample (ZnO-A to ZnO-E) were 0.00727, 0.00659, 0.00465, 0.00397, and 0.00602 (Eq. (2)). These values confirm the uniformity of the specimen in all crystallographic directions. A slight shift towards a lower Bragg angle indicates the presence of constant strain in the crystal (Fig. 1), as well as changes in the intensity and widening of the diffraction peaks representing the rearrangement of the crystal planes according to the synthesis conditions [43].

Dislocation densities of ZnO-A to ZnO-E, which are calculated using Eq. (3), namely 0.00432, 0.00355, 0.00175, 0.00127, and 0.00293. It can be seen that FWHM, lattice strain, and dislocation density show the same behavior and tendency, fluctuating when the molarity of NaOH changes from 1.25 to 5 mol/L or the pH value changes from 11 to 14. These fluctuations are influenced by the molarity of NaOH, where a lower molarity gives a crystallite size smaller and larger grain boundary areas that constrain dislocation densities. Consequently, a grain size reduction usually increases the nanoparticles' toughness and lowers the dislocation density [46]. According to Abdulrahman et al. [45], fluctuations in dislocation density and FWHM are caused by variations in crystallite size and the internal strain formed by lattice mismatch and ZnO NPs aggregation with each other at higher pH values. This means that the pH value significantly affects the final product of different nanostructures. The contribution of a higher pH makes the FWHM value smaller and provides a sufficient amount of OH^- presence to form ZnO.

XRD diffractogram analysis proved that changes in the molarity of NaOH had increased the crystalline properties of ZnO. The effect is expressed in a decrease in the width of the diffraction peaks and, consequently, in the lattice strain, which also decreases based on the calculation of the lattice parameters [50]. The high and sharp intensity of the diffraction peaks is related to the degree of crystallinity and the position of the atoms in the unit cell. Shifting atomic positions results in increasing or decreasing the peak intensity of the XRD diffractogram, which has an impact on the distance between the planes, as shown in Table 1 [51].

Quantitative analysis

Quantitative analysis of XRD data was carried out using Rietveld's Rietica software to refine data. The model used to refine information is PDF No. 01-089-0510. In general, the refinement results in all samples were good, so the model used can represent the success of ZnO NPs synthesis. After a series of refinements, cell parameters of synthesized ZnO NPs can be seen in Table 2. The standard cell parameters for refining data are ICSD collection code 82028 with values a = b = 3.249 Å and c = 5.205 Å. This change is due to increasing the

Table 2. Cell parameters for XRD patterns of ZnO NPs after refinement

Samples	a = b (Å)	c (Å)	Lattice distortion (c/a)	Cell volume (Å^3)
ZnO-A	3.249	5.203	1.601	54.923
ZnO-B	3.250	5.207	1.602	54.999
ZnO-C	3.256	5.216	1.602	55.298
ZnO-D	3.249	5.205	1.602	54.944
ZnO-E	3.195	5.103	1.597	52.092

molarity of NaOH given to the sample, which causes changes in cell volume, cell parameters (a = b and c), and crystallite size. Differences in lattice parameters and unit cell volume were observed among samples ZnO-A, ZnO-B, ZnO-C, and ZnO-D. Variation in the molarity of NaOH in the synthesized ZnO NPs has changed the cell volume. These results indicate that NaOH affects the growth of ZnO NPs crystals by controlling the growth conditions [52]. The reaction of NaOH in zinc nitrate solution plays an essential role in the crystallization process. Adding NaOH mass causes the supersaturation state that occurs during the synthesis to increase. Supersaturation is the driving force for crystal nucleation and growth [45,52].

The reduction in cell volume in the ZnO-A, ZnO-B, and ZnO-C samples was caused by differences in the molarity of NaOH in the zinc nitrate solution. The temperature gradient is created by a certain molarity of NaOH in the zinc nitrate solution, which accelerates the nucleation process [53]. Crystal nucleation is more dominant than crystal growth because the supersaturation state increases after adding NaOH mass, which increases the pH of the solution. In contrast, crystal growth at low supersaturation is faster than nucleation, so the crystallite size becomes more significant. Jay Chithra et al. [54], in their research, obtained that the morphology of ZnO nanoparticles changed from a coarse structure to rod-like when the pH of the solution increased. These morphological changes indicate that increasing the pH has a greater impact on the morphology of the ZnO NPs. The crystallite size, morphology, phase, and surface area of ZnO NPs highly depend on the number of positively and negatively charged ions present in the medium during preparation. The pH conditions of the medium can change the electrical charge of the molecules, and this change will affect their reduction [55].

Fig. 2 shows typical different plots measured (black) and calculated patterns (red) for samples ZnO-A and ZnO-E. The green color is the difference in intensity between the two, while the vertical blue lines indicate the diffraction peaks. The refinement process succeeded in analyzing the measured pattern and the calculated pattern. This means that the prepared ZnO NPs follow the reference results, also indicated by the decrease in the reliability (R) factors (R_p, R_{wp}, R_{exp}, and R_B) and goodness of fit (GOF) during the calculation process. The R factor and GOF values are shown in Table 3. Fig. 2(a) and Fig. 2(b) compare the results of refined samples obtained from

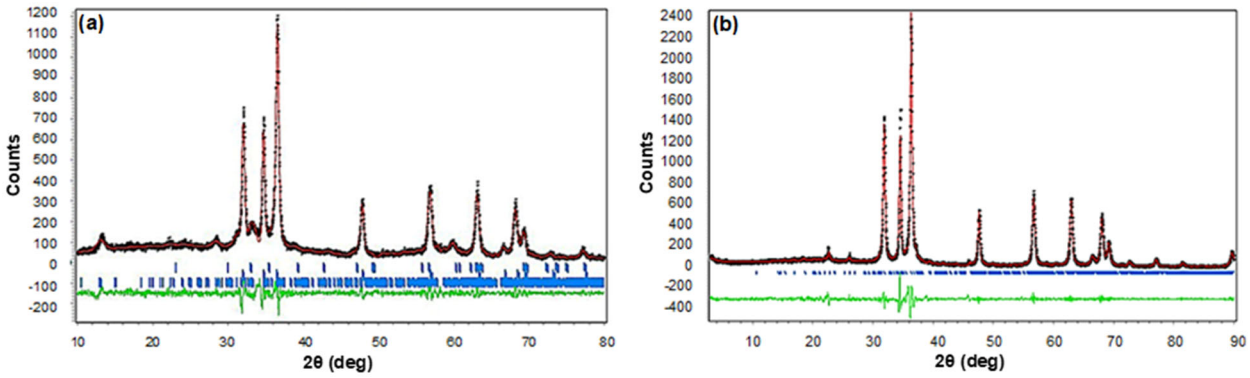

Fig 2. Rietveld refinement of XRD patterns of ZnO NPs (a) ZnO-A; and (b) ZnO-E

Table 3. R and GoF suitability factors, resulting from refinement of XRD data for ZnO-A and ZnO-E samples

Samples	R_p	R_{wp}	R_{exp}	GoF	R_{Bragg}
ZnO-A	8.43	11.01	10.32	1.130	0.49
ZnO-E	9.33	12.93	9.50	1.852	1.33

chemical synthesis (ZnO-A, NaOH = 1.25 mol/L) and biosynthesis with MLE (ZnO-E, NaOH = 0.25 mol/L). The diffractogram of Fig. 2 shows several peaks other than the prominent ZnO peak, representing a phase other than ZnO NPs. It is thought that the nitrate compounds not dissolved during synthesis contributed to this diffraction peak (Fig. 2(a)). In contrast, the cellulose compounds contributed to the MLE biosynthetic diffractogram (Fig. 2(b)).

SEM Analysis

The surface morphology of the ZnO NPs was studied further using SEM, whose images are presented in Fig. 3. SEM images of ZnO NPs obtained are generally agglomerated conditions and reveal nanostructure information that shapes rod-like, are thought to be formed due to NaOH adsorbed on the ZnO core. Generally, variations in the mass of NaOH showed a change in the crystallite size as the mass of NaOH added increased. Sample ZnO-A (Fig. 3(a)) was shaped like a sheet [56], sample ZnO-D (Fig. 3(b)), such as needles and granular grains, and sample ZnO-E (Fig. 3(c)), such as flower-like. The different surface morphologies of the samples are due to lattice mismatch, chemical bonding across the interface, and the presence of residual oxides. Based on Fig. 3 with the same magnification, visually, the grain size of the synthesized ZnO NPs decreased with the addition of NaOH. All samples showed agglomerated morphology and were not in a uniform shape. This is because the changes in phase pH due to NaOH mass to alkaline sol may cause agglomeration. Based on some literature [57-59], crystallite formation occurs when the number of OH^- ions are sufficient for the nucleation and growth of ZnO NPs. In Fig. 3(a), the crystallite formed at pH 11 shows high agglomeration because the OH^- ions from NaOH are not enough to form ZnO NPs. In contrast, the ZnO NPs particles in Fig. 3(b) (pH 14) showed a uniform rice-like and some rod-like distribution, indicating complete ZnO NPs formation. Interestingly, several very small nanorods on the lateral surface of a single pencil-like stem (Fig. 3(b)) make ZnO NPs look like a thorny flower. The nanorods grow almost vertically on the lateral surface of the pencil-like stem, which is induced by secondary nucleation. In addition, as reported by Sounart et al. [60], nuclei aligned in the most energetically favorable orientation grow at the expense of misaligned nuclei due to reduced interfacial pressure on the primary ZnO surface. Other factors might also contribute to nucleation, such as the adsorption of the diamines on the ZnO crystal. Diaminoalkane molecules regulate secondary nucleation at concentrations of Zn that approach the saturation point in the growth of secondary branches. The organic diamines control the nucleation and growth of branches through their influence on ZnO solubility by forming Zn-amino complexes and pH. From morphological studies, the effect of increasing the pH value or increasing the molarity of NaOH will cause the formation of grain size to decrease.

Fig. 3(c) reveals the effect of MLE on the morphology of ZnO NPs, which forms a cauliflower-like

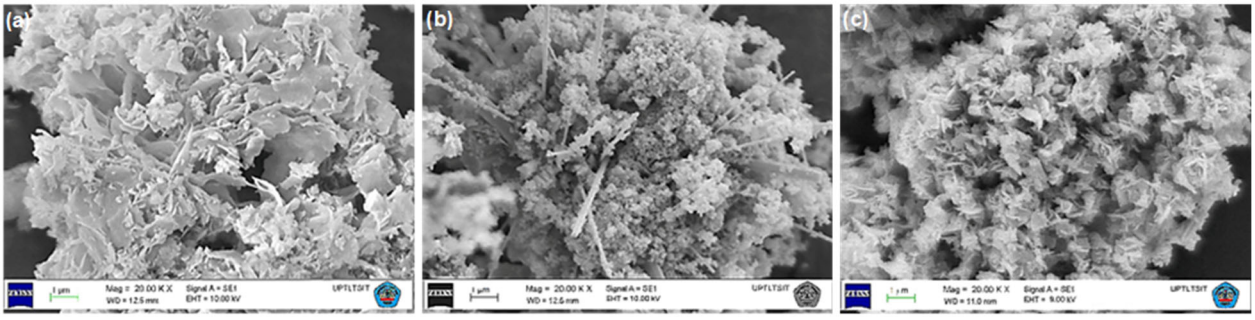

Fig 3. SEM image for ZnO NPs, that is, ZnO-A (a), ZnO-D (b), and ZnO-E (c). Bar scale = 1 μm. Magnification = 20,000×

shape [14]. Mango (*M. indica*) leaves have biomolecules (like carbohydrates, proteins, and coenzymes) that can reduce metal salt into nanoparticles. The phytochemicals (flavones, terpenoids, sugars, ketones, aldehydes, carboxylic acids, and amides) in MLE can potentially reduce metal ions in a short incubation time due to acting as both reducing and stabilizing agents in the ZnO NPs synthesis process [61]. Flavonoids contain various functional groups, which have an enhanced ability to reduce metal ions. The reactive hydrogen atom is released due to tautomeric transformations in flavonoids by which enol-form is converted into the keto-form. This process is realized by the reduction of metal ions into metal nanoparticles. However, Fig. 3 can confirm the results of the ZnO NPs XRD diffractogram in Table 2, where the effect of the NaOH on peak widening causes the crystallite size to increase while the lattice strain decreases (Eq. (2)).

TEM Analysis

The internal morphology of ZnO NPs is known through the TEM micrograph (Fig. 4), confirming the agglomeration of ZnO NPs (Fig. 3), and some of the particles are not entirely separated. TEM micrograph also shows the presence of various hexagonal structures in the sample, especially in ZnO-D (Fig. 4(a)).

ZnO-D (Fig. 4(a)) has a non-uniform rod-like structure. ZnO-D has an average diameter distribution of 30 nm, while ZnO-E (Fig. 4(b)) has an average size of 20 nm after being analyzed using ImageJ software. Several studies [62-64] show that nanorods can be obtained by the hydrothermal synthesis method. The TEM image in Fig. 4(b) shows the nanoflowers (Fig. 3(c)), which are non-uniformly assembled. It displays dispersed ZnO nanoparticles with a semi-spherical shape. The nanoflowers appear agglomerated and overlapping due to their intersection [56].

FTIR Analysis

FTIR has been used to test the purity and properties of ZnO NPs with the pattern shown in Fig. 5. ZnO NPs have been synthesized by hydrothermal method and obtained FTIR pattern with characteristic peaks (Fig. 5(a)). The peak at ~3347 cm^{-1} is due to O–H stretching assigned to water absorption on metal surfaces [65]. The peak at ~2102 cm^{-1} is present in all samples. It can be attributed to atmospheric CO_2 uptake of metal cations that may be present in the apparatus during analysis [66]. Another possibility is due to the high surface area of ZnO NPs, which absorb water rapidly from the atmosphere when the samples are kept and ground in the air [67].

Narrow peaks at 1498 and 1386 cm^{-1} can be set to nitrate ions due to unreacted zinc nitrate residues [68]. It is known that the typical vibrational band of nitrate is usually in the range of 1200 to 1500 cm^{-1} [69]. This peak corresponds to the Rietveld pattern (Fig. 2(a)), which has a small peak of 2θ around 13.2°. These peaks disappeared after the mass of NaOH was added to the solution. The absorption band at 870 cm^{-1} is assigned C–O deformation vibrations in the plane [70]. The asymmetric stretching

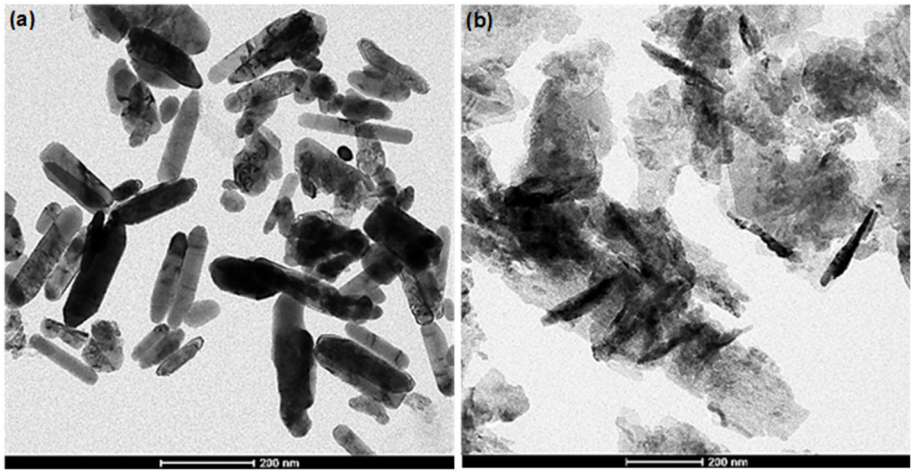

Fig 4. TEM image for ZnO NPs, namely ZnO-D (a) and ZnO-E (b). Bar scale: 200 nm

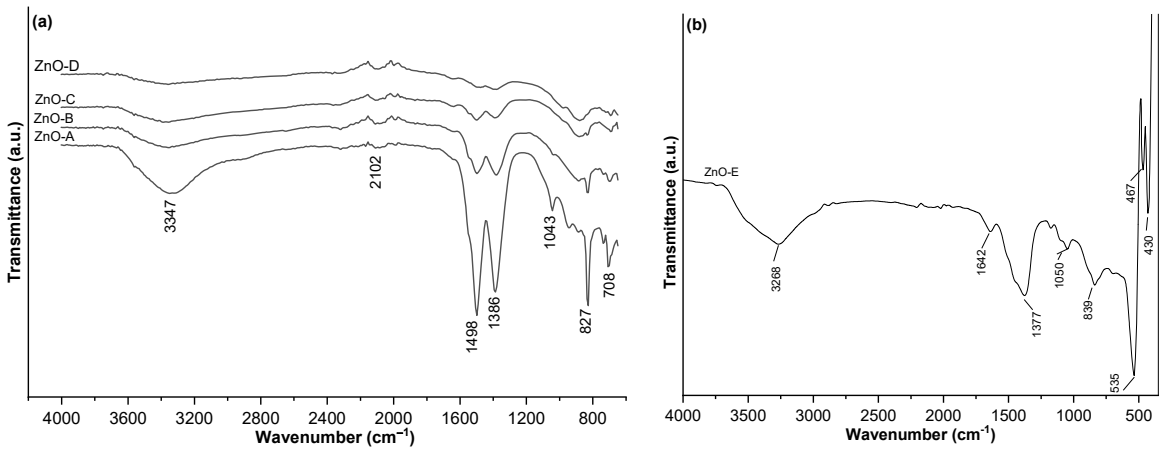

Fig 5. FTIR pattern of ZnO NPs synthesized by (a) hydrothermal method with variation of NaOH mass, and (b) biosynthesis using MLE

vibration of C–O vibration of bound C–OH is observed at 1043 cm^{-1} [65,69]. The more NaOH added, the more precipitated $Zn(OH)_2$ dissolved and formed a homogeneous aqueous solution that contained ions. During the supersaturation process, it is assumed that the ions act as a growth unit for the ZnO nucleus to combine into the ZnO crystallite [71]. This process increases the size of the crystallites, as shown in Table 2. The peaks at wavenumbers ~655 and ~800 cm^{-1} are typical vibrational modes of Zn–O in the infrared region [66,72], confirming the presence of ZnO NPs.

Fig. 5(b) reveals the FTIR pattern of ZnO NPs with infrared absorption at wavenumber 400–4000 cm^{-1}. The presence of peaks at 430, 467, and 535 cm^{-1}, characteristic of the Zn–O bond signal, confirms that this sample is indeed ZnO [27,73]. In addition, the functional group of aromatic rings is linked to the bands 1642, 1377, and 839 cm^{-1} [28], which are functional groups of organic compounds in the MLE. According to Nava et al. [73], the presence of this group in organic compounds will differ in various parts of the extracted plant. However, this group indicates that phenolic compounds, flavonoids, and other phytochemical compounds in MLE can trigger the reduction and stabilization of zinc salts and ZnO NPs size in aqueous medium [28-29]. The strong absorption peak at 3268 cm^{-1} was attributed to the O–H stretching of alcohols and phenols [28], and the amine group of the N–H bond vibrations in MLE [17,27], which caused water adsorption on the ZnO NPs surface. This group is associated with alkaloids where the peak shift and intensity are related to the interaction with ZnO NPs. The functional groups in the extract donate electrons, which can reduce zinc ions (Zn^{2+} to Zn^{+}) and, finally, Zn^{0}, while the negative functional groups have a stabilizing effect [30].

Band Gap Energy Analysis

The UV-vis data recording at 200–800 nm was carried out, but in Fig. 6, the UV-vis absorption spectrum of the synthesized ZnO NPs was captured at 200–600 nm. The UV-vis absorption spectrum of the ZnO NP structure is shown in Table 3, where the excitonic absorption peak is lower than the value reported

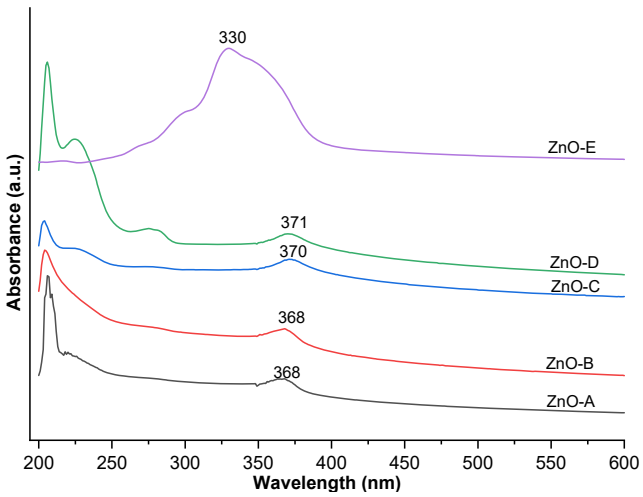

Fig 6. UV-vis data spectrum of the synthesized ZnO NPs, with excitonic absorption peaks

Table 3. Band gap energy of ZnO NPs based on UV-vis DRS instrument

Samples	Absorption peaks (nm)	Band gap energy E_g (eV)
ZnO-A	368	3.25
ZnO-B	368	3.25
ZnO-C	370	3.26
ZnO-D	371	3.31
ZnO-E	330	3.17

for bulk ZnO, which is 388 nm. The absorption peaks are referred to as electron transitions between the intrinsic defect levels and between the valence and conduction bands [74]. E_g is obtained using Eq. (4) as in Table 3.

The band gap energy variations that occur after being synthesized with different molarity of NaOH are related to the crystal quality (FWHM) of the ZnO nanostructures, for example, dislocation density, impurities, internal strain, and thickness, which XRD results have investigated. These values (ZnO-A to ZnO-D) are the same as the previous research report [56] but lower than the E_g bulk ZnO value (3.37 eV). The UV-vis absorption results show a blue shift in the typical absorption peak with a decrease in the crystallite size of the nanostructure, attributed to the quantum confinement effect on the synthesized sample [74]. According to Agarwal et al. [56] and Köseoğlu [75], crystallite size, morphology, and synthesis method of ZnO NPs affect the width of the resulting band gap energy. In addition, the changes in E_g can be explained from the point of view of the defects present on the surface and the type of absorption [49].

In Table 3, ZnO-E has an absorption value of UV-vis of 330 nm. The transfer of electrons from the valence band to the conduction band causes the formation of a ZnO NPs absorption spectrum with an excitation band at the peak of 330 nm (E_g is 3.17 eV using the Tauc Plot). The value of this band gap energy is in the range of reported values of ZnO NPs [26]. It is well known that the variation in band gap energy can be due to a structural parameter and to the size of the grains. The blue shift at the absorption edge towards a lower wavelength indicates a higher energy requirement to induce a photocatalytic effect on ZnO NPs [75]. The presence of broad peaks in the UV-vis spectrum indicates excellent optical properties of the ZnO NPs synthesized with green synthesis [27], especially using MLE. In addition, the absorption spectra of the ZnO NPs showed limited dispersion of the NPs. The observed optical bandgap revealed that the synthesized ZnO NPs had inherited excellent electron transaction and photocatalytic capabilities.

The mechanism for the formation of ZnO NPs is based on the reaction between Zn^{2+} ions in solution with polyphenols and flavonoids present in MLE to form complex $ZnOH_4^{2-}$ which is grown in a strongly alkaline solution. Furthermore, a hydrolysis reaction is carried out to form zinc hydroxide due to the presence of hydroxyl groups in polyphenols or flavonoids. ZnO NPs particles form during a heating or calcination reaction that accumulates ZnO NPs crystallites. This process has revealed the presence of chemical compounds (phenols and flavonoids) in *M. indica* leaves, which act as reducing and stabilizing agents by reducing zinc ions to the 0-valence state [31,76].

Photocatalytic Analysis

The effect of ZnO-E photocatalyst to degrade MB for 90 min is shown in Fig. 7. The photocatalytic activity of ZnO-E was evaluated through the photodegradation of MB under sunlight. The photocatalyst was then exposed to sunlight for 90 min at a temperature of 34 °C. The UV-vis absorption spectrum of MB versus time for ZnO-E is shown in Fig. 7(a).

Spectrum data for the aqueous solution of the MB molecule shows two peaks, 663 and 616 nm, which correspond to the monomer and dimer, respectively [26]. The presence of ZnO-E caused the absorbance of MB to decrease sharply after 60 min. This was revealed from changes in absorption peaks at 663 and 616 nm after 60 min, which showed that the degradation rate of monomers was much higher than dimers.

The decrease in MB concentration with respect to time for ZnO-E is shown in Fig. 7(b). As shown in Fig. 7(a), MB degraded almost completely after irradiation for 90 min by ZnO-E. The MB degradation rate proves the excellent performance of ZnO-E. These results are consistent with the textural properties of the ZnO-E photocatalyst, namely, the crystallite size is small, and the

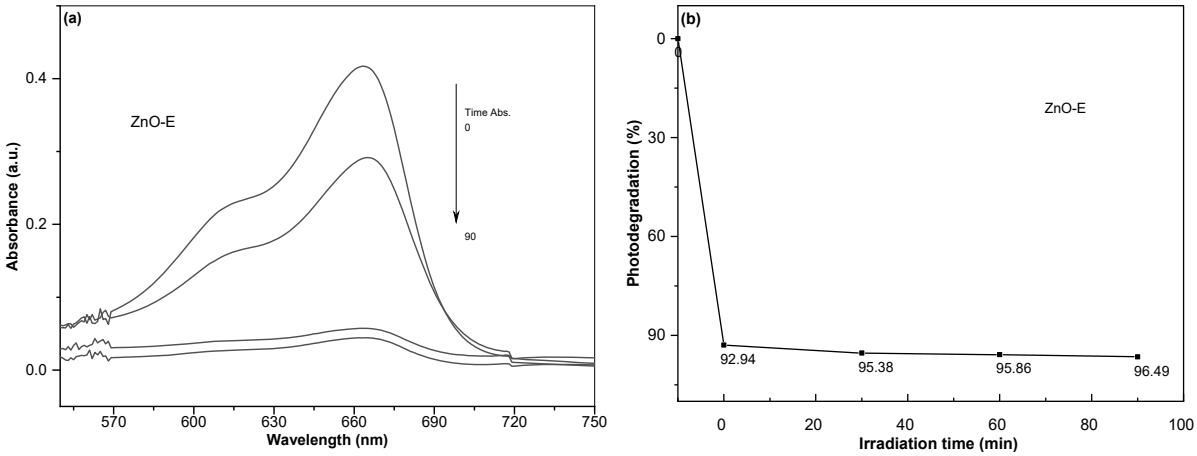

Fig 7. Photocatalytic activity of the ZnO-E photocatalyst material; percentage of MB color degradation (a), and reaction kinetics orde-1 (b)

surface area is large. The implication is that the degradation of MB dyes is quickly due to the large number of reactions that co-occur. This is following research [77-78] which states that there is an effect of the surface profile on the photoactivity of the photocatalytic material. Using Eq. (4) and (5), the reaction rate is 0.0954 ppm/min, and the photodegradation is 96.46% after 90 min. Photodegradation of MB by using ZnO-E corresponds to the results of [26], who synthesized ZnO NPs using *Rosmarinus officinalis* leaf extract.

■ CONCLUSION

ZnO NPs have been successfully synthesized chemically and bio-chemically (biosynthesis) using $Zn(NO_3)_2{\cdot}6H_2O$ (precursor), NaOH (reducing agent), and MLE (capping and stabilizing agents). The synthesized ZnO NPs were agglomerated and varied in size and shape, namely 15.2, 16.8, 23.9, 28.2 and 18.4 nm, respectively. XRD patterns and FTIR spectra showed the formation of hexagonal wurtzite structures in all synthesized ZnO NPs. For biosynthesis using MLE, the FTIR pattern indicated the presence of chemical compounds in the leaves that contributed to the formation of ZnO NPs crystallites. The variation in crystallite size revealed differences in the obtained band gap energy, namely 3.25, 3.25, 3.26, 3.31, and 3.17 eV. ZnO-A and ZnO-B, with the same crystallite size, showed the same band gap energy for the absorption of UV light. In ZnO-C and ZnO-D, the difference in crystallite size was quite significant, and the band gap energy for absorbing UV was close to the ZnO bulk value. In ZnO-E, the band gap energy is related to the wavelength of UV light absorption (330 nm). The capability of ZnO-E, synthesized using MLE, is demonstrated by the photodegradation rate of 96.46% when used as a photocatalyst. An alternative reference for the production of environmentally friendly ZnO nanoparticles for MB dye photocatalysis applications can be offered by this.

■ ACKNOWLEDGMENTS

Thank you for the support from the research grant for the Doctoral Dissertation Program, organized by the Ministry of Education, Culture, Research and Technology of the Republic of Indonesia in collaboration with the Research Institute and Community Service, University of Lampung. The number of the contract is 027/E5/PG.02.00/PT/2022.

■ AUTHOR CONTRIBUTIONS

The first author (Sri Wahyu Suciyati), as a researcher, carried out data collection and writing original draft preparation. The second author (Posman Manurung) is the corresponding author and writing-review and editing. The third (Junaidi) and fourth authors (Rudy Situmeang) served as writing-review and conducting revisions. All authors have read and agreed to the published version of the manuscript.

REFERENCES

[1] Espitia, P.J.P., Soares, N.F.F., Coimbra, J.S.R., de Andrade, N.J., Cruz, R.S., Medeiros, E.A.A., 2012, Zinc oxide nanoparticles: Synthesis, antimicrobial activity and food packaging applications, *Food Bioprocess Technol.*, 5 (5), 1447–1464.

[2] Lu, P.J., Fang, S.W., Cheng, W.L., Huang, S.C., Huang, M.C., and Cheng, H.F., 2018, Characterization of titanium dioxide and zinc oxide nanoparticles in sunscreen powder by comparing different measurement methods, *J. Food Drug Anal.*, 26 (3), 1192–1200.

[3] Amini, M., and Ashrafi, M., 2016, Photocatalytic degradation of some organic dyes under solar light irradiation using TiO_2 and ZnO nanoparticles, *Nanochem. Res.*, 1 (1), 79–86.

[4] Siddiqi, K.S., ur Rahman, A., Tajuddin, T., and Husen, A., 2018, Properties of zinc oxide nanoparticles and their activity against microbes, *Nanoscale Res. Lett.*, 13 (1), 141.

[5] Ungureanu, N., Biriş, S.S., Vlăduţ, V., Zăbavă, B., and Popa, M., 2019, TiO_2 photocatalyst in wastewater treatment – review, *International Symposium ISB-INMATEH – Agricultural and Mechanical Engineering*, Bucharest, Romania, 31 October-1 November 2019.

[6] Elfeky, A.S., Youssef, H.F., and Elzaref, A.S., 2020, Adsorption of dye from wastewater onto ZnO nanoparticles-loaded zeolite: Kinetic, thermodynamic and isotherm studies, *Z. Phys. Chem.*, 234 (2), 255–278.

[7] Barnes, R.J., Molina, R., Xu, J., Dobson, P.J., and Thompson, I.P., 2013, Comparison of TiO_2 and ZnO nanoparticles for photocatalytic degradation of methylene blue and the correlated inactivation of gram-positive and gram-negative bacteria, *J Nanoparticle Res.*, 15 (2), 1432.

[8] Ayanda, O.S., Adeleye, B.O., Aremu, O.H., Ojoloba, F.B., Lawal, O.S., Amodu, O.S., Oketayo, O.O., Klink, M.J., and Nelana, S.M., 2023, Photocatalytic degradation of metronidazole using zinc oxide nanoparticles supported on acha waste, *Indones. J. Chem.*, 23 (1), 158–169.

[9] Jiang, W., Mashayekhi, H., and Xing, B., 2009, Bacterial toxicity comparison between nano- and micro-scaled oxide particles, *Environ. Pollut.*, 157 (5), 1619–1625.

[10] Qamar, M., and Muneer, M., 2009, A comparative photocatalytic activity of titanium dioxide and zinc oxide by investigating the degradation of vanillin, *Desalination*, 249 (2), 535–540.

[11] Adams, L.K., Lyon, D.Y., and Alvarez, P.J.J., 2006, Comparative eco-toxicity of nanoscale TiO_2, SiO_2, and ZnO water suspensions, *Water Res.*, 40 (19), 3527–3532.

[12] Jeong, B., Kim, D.H., Park, E.J., Jeong, M.G., Kim, K.D., Seo, H.O., Kim, Y.D., and Uhm, S., 2014, ZnO shell on mesoporous silica by atomic layer deposition: Removal of organic dye in water by an adsorbent and its photocatalytic regeneration, *Appl. Surf. Sci.*, 307, 468–474.

[13] Zhang, W., Meng, L., Mu, G., Zhao, M., Zou, P., and Zhang, Y., 2016, A facile strategy for fabrication of nano-ZnO/yeast composites and their adsorption mechanism towards lead(II) ions, *Appl. Surf. Sci.*, 378, 196–206.

[14] Monsef Khoshhesab, Z., and Souhani, S., 2018, Adsorptive removal of reactive dyes from aqueous solutions using zinc oxide nanoparticles, *J. Chin. Chem. Soc.*, 65 (12), 1482–1490.

[15] Adam, F., Himawan, A., Aswad, M., Ilyas, S., Heryanto, H., Anugrah, M.A., and Tahir, D., 2021, Green synthesis of zinc oxide nanoparticles using *Moringa oleifera* L. water extract and its photocatalytic evaluation, *J. Phys.: Conf. Ser.*, 1763 (1), 012002.

[16] Rajeshkumar, S., Kumar, S.V., Ramaiah, A., Agarwal, H., Lakshmi, T., and Roopan, S.M., 2018, Biosynthesis of zinc oxide nanoparticles using *Mangifera indica* leaves and evaluation of their antioxidant and cytotoxic properties in lung cancer (A549) cells, *Enzyme Microb. Technol.*, 117, 91–95.

[17] Narayana, A., Pandey, K., Azmi, N., Tejashwini, M., Shrestha, U., and Lokesh, S.V., 2018, Synthesis and characterization of zinc oxide (ZnO) nanoparticles

using mango (*Mangifera indica*) leaves, *Int. J. Res. Anal. Rev.*, 5 (3), 17–23.

[18] Kumaresan, N., Ramamurthi, K., Ramesh Babu, R., Sethuraman, K., and Moorthy Babu, S., 2017, Hydrothermally grown ZnO nanoparticles for effective photocatalytic activity, *Appl. Surf. Sci.*, 418, 138–146.

[19] Kumar, S.G., and Rao, K.S.R.K., 2015, Zinc oxide based photocatalysis: Tailoring surface-bulk structure and related interfacial charge carrier dynamics for better environmental applications, *RSC Adv.*, 5 (5), 3306–3351.

[20] Franco, P., Sacco, O., De Marco, I., and Vaiano, V., 2019, Zinc oxide nanoparticles obtained by supercritical antisolvent precipitation for the photocatalytic degradation of crystal violet dye, *Catalysts*, 9 (4), 346.

[21] Uysal, B., Şen, S., and Top, A., 2020, Photocatalytic and optical properties of zinc oxide structures prepared at different urea concentrations, *Rev. Rom. Mater.*, 50 (4), 463–470.

[22] Wibowo, A., Marsudi, M.A., Amal, M.I., Ananda, M.B., Stephanie, R., Ardy, H., and Diguna, L.J., 2020, ZnO nanostructured materials for emerging solar cell applications, *RSC Adv.*, 10 (70), 42838–42859.

[23] Akhoon, S.A., Rubab, S., and Shah, M.A., 2015, A benign hydrothermal synthesis of nanopencils-like zinc oxide nanoflowers, *Int. Nano Lett.*, 5 (1), 9–13.

[24] Kolodziejczak-Radzimska, A., and Jesionowski, T., 2014, Zinc oxide—From synthesis to application: A review, *Materials*, 7 (4), 2833–2881.

[25] Satheshkumar, M., Anand, B., Muthuvel, A., Rajarajan, M., Mohana, V., and Sundaramanickam, A., 2020, Enhanced photocatalytic dye degradation and antibacterial activity of biosynthesized ZnO-NPs using curry leaves extract with coconut water, *Nanotechnol. Environ. Eng.*, 5 (3), 29.

[26] Saad Algarni, T., Abduh, N.A.Y., Al Kahtani, A., and Aouissi, A., 2022, Photocatalytic degradation of some dyes under solar light irradiation using ZnO nanoparticles synthesized from *Rosmarinus officinalis* extract, *Green Chem. Lett. Rev.*, 15 (2), 460–473.

[27] Hussain, A., Oves, M., Alajmi, M.F., Hussain, I., Amir, S., Ahmed, J., Rehman, M.T., El-Seedi, H.R., and Ali, I., 2019, Biogenesis of ZnO nanoparticles using *Pandanus odorifer* leaf extract: Anticancer and antimicrobial activities, *RSC Adv.*, 9 (27), 15357–15369.

[28] Nagajyothi, P.C., Cha, S.J., Yang, I.J., Sreekanth, T.V.M., Kim, K.J., and Shin, H.M., 2015, Antioxidant and anti-inflammatory activities of zinc oxide nanoparticles synthesized using *Polygala tenuifolia* root extract, *J. Photochem. Photobiol., B*, 146, 10–17.

[29] Soto-Robles, C.A., Luque, P.A., Gómez-Gutiérrez, C.M., Nava, O., Vilchis-Nestor, A.R., Lugo-Medina, E., Ranjithkumar, R., and Castro-Beltrán, A., 2019, Study on the effect of the concentration of *Hibiscus sabdariffa* extract on the green synthesis of ZnO nanoparticles, *Results Phys.*, 15, 102807.

[30] Alamdari, S., Sasani Ghamsari, M., Lee, C., Han, W., Park, H.H., Tafreshi, M.J., Afarideh, H., and Ara, M.H., 2020, Preparation and characterization of zinc oxide nanoparticles using leaf extract of *Sambucus ebulus*, *Appl. Sci.*, 10 (10), 3620.

[31] Chemingui, H., Missaoui, T., Mzali, J.C., Yildiz, T., Konyar, M., Smiri, M., Saidi, N., Hafiane, A., and Yatmaz, H.C., 2019, Facile green synthesis of zinc oxide nanoparticles (ZnO NPs): Antibacterial and photocatalytic activities, *Mater. Res. Express*, 6 (10), 1050b4.

[32] Sierra, M.J., Herrera, A.P., and Ojeda, K.A., 2018, Synthesis of zinc oxide nanoparticles from mango and soursop leaf extracts, *Contemp. Eng. Sci.*, 11 (8), 395–403.

[33] Rajeshkumar, S., Parameswari, R.P., Sandhiya, D., Al-Ghanim, K.A., Nicoletti, M., and Govindarajan, M., 2023, Green synthesis, characterization and bioactivity of *Mangifera indica* seed-wrapped zinc oxide nanoparticles, *Molecules*, 28 (6), 2818.

[34] Kumar, M., Saurabh, V., Tomar, M., Hasan, M., Changan, S., Sasi, M., Maheshwari, C., Prajapati, U., Singh, S., Prajapat, R.K., Dhumal, S., Punia, S., Amarowicz, R., and Mekhemar, M., 2021, Mango (*Mangifera indica* L.) leaves: Nutritional

composition, phytochemical profile, and health-promoting bioactivities, *Antioxidants*, 10 (2), 299.

[35] Wijesinghe, U., Thiripuranathar, G., Menaa, F., Iqbal, H., Razzaq, A., and Almukhlifi, H., 2021, Green synthesis, structural characterization and photocatalytic applications of ZnO nanoconjugates using *Heliotropium indicum*, *Catalysts*, 11 (7), 0831.

[36] El-Hossary, F.M., Abd El-Rahman, A.M., Abdelhamidshahat, M., and Ebnalwaled, A.A., 2018, Low hydrothermal temperature synthesis and characterization of ZnO nanoparticles, *Int. J. Latest Res. Eng. Technol.*, 4 (4), 45–51.

[37] Batterjee, M.G., Nabi, A., Kamli, M.R., Alzahrani, K.A., Danish, E.Y., and Malik, M.A., 2022, Green hydrothermal synthesis of zinc oxide nanoparticles for UV-light-induced photocatalytic degradation of ciprofloxacin antibiotic in an aqueous environment, *Catalysts*, 12 (11), 1347.

[38] Tanwar, S., and Mathur, D., 2021, Hydrothermal synthesis and characterization of zinc oxide nanoplates, *Mater. Today: Proc.*, 47, 4647–4651.

[39] Moharram, A.H., Mansour, S.A., Hussein, M.A., and Rashad, M., 2014, Direct precipitation and characterization of ZnO nanoparticles, *J. Nanomater.*, 2014, 716210.

[40] Mote, V.D., Purushotham, Y., and Dole, B.N., 2012, Williamson-Hall analysis in estimation of lattice strain in nanometer-sized ZnO particles, *J. Theor. Appl. Phys.*, 6 (1), 6.

[41] Agus Sumiarna, G.P., Irmansyah, I., and Maddu, A., 2016, Dye-sensitized solar cell based on flower-like ZnO nanoparticles as photoanode and natural dye as photosensitizer, *J. Nano- Electron. Phys.*, 8 (2), 02012.

[42] Sawada, H., Wang, R., and Sleight, A.W., 1996, An electron density residual study of zinc oxide, *J. Solid State Chem.*, 122 (1), 148–150.

[43] Koutu, V., Shastri, L., and Malik, M.M., 2016, Effect of NaOH concentration on optical properties of zinc oxide nanoparticles, *Mater. Sci.-Pol.*, 34 (4), 819–827.

[44] Amin, G., Asif, M.H., Zainelabdin, A., Zaman, S., Nur, O., and Willander, M., 2011, Influence of pH, precursor concentration, growth time, and temperature on the morphology of ZnO nanostructures grown by the hydrothermal method, *J. Nanomater.*, 2011, 269692.

[45] Abdulrahman, A.F., Ahmed, S.M., Hamad, S.M., Almessiere, M.A., Ahmed, N.M., and Sajadi, S.M., 2021, Effect of different pH values on growth solutions for the ZnO nanostructures, *Chin. J. Phys.*, 71, 175–189.

[46] Nath, M.R., Ahmed, A.N., Gafur, M.A., Miah, M.Y., and Bhattacharjee, S., 2018, ZnO nanoparticles preparation from spent zinc–carbon dry cell batteries: Studies on structural, morphological and optical properties, *J. Asian Ceram. Soc.*, 6 (3), 262–270.

[47] Lu, C.H., and Yeh, C.H., 2000, Influence of hydrothermal conditions on the morphology and particle size of zinc oxide powder, *Ceram. Int.*, 26 (4), 351–357.

[48] Mohammadi, F.M., Ghasemi, N., 2018, Influence of temperature and concentration on biosynthesis and characterization of zinc oxide nanoparticles using cherry extract, *J. Nanostruct. Chem.*, 8 (1), 93–102.

[49] Duraimurugan, J., Kumar, G.S., Maadeswaran, P., Shanavas, S., Anbarasan, P.M., and Vasudevan, V., 2019, Structural, optical and photocatalytic properties of zinc oxide nanoparticles obtained by simple plant extract mediated synthesis, *J. Mater. Sci.: Mater. Electron.*, 30 (2), 1927–1935.

[50] Khorsand Zak, A., Razali, R., Abd Majid, W.H.B., and Darroudi, M., 2011, Synthesis and characterization of a narrow size distribution of zinc oxide nanoparticles, *Int. J. Nanomed.*, 6, 1399–1403.

[51] Cullity, B.D., and Stock, S.R., 2014, *Elements of X-Ray Diffraction*, 3rd Ed., Pearson India Education Services, India.

[52] Bindu, P., and Thomas, S., 2014, Estimation of lattice strain in ZnO nanoparticles: X-ray peak profile analysis, *J. Theor. Appl. Phys.*, 8 (4), 123–134.

[53] Xu, S., and Wang, Z.L., 2011, One-dimensional ZnO nanostructures: Solution growth and functional properties, *Nano Res.*, 4 (11), 1013–1098.

[54] Jay Chithra, M., Sathya, M., and Pushpanathan, K., 2015, Effect of pH on crystal size and

photoluminescence property of ZnO nanoparticles prepared by chemical precipitation method, *Acta Metall. Sin. (Engl. Lett.)*, 28 (3), 394–404.

[55] Hasan, M., Ullah, I., Zulfiqar, H., Naeem, K., Iqbal, A., Gul, H., Ashfaq, M., and Mahmood, N., 2018, Biological entities as chemical reactors for synthesis of nanomaterials: Progress, challenges and future perspective, *Mater. Today Chem.*, 8, 13–28.

[56] Agarwal, S., Jangir, L.K., Rathore, K.S., Kumar, M., and Awasthi, K., 2019, Morphology-dependent structural and optical properties of ZnO nanostructures, *Appl. Phys. A: Mater. Sci. Process.*, 125 (8), 553.

[57] Ribut, S.H., Che Abdullah, C.A., Mustafa, M., Mohd Yusoff, M.Z., and Ahmad Azman, S.N., 2019, Influence of pH variations on zinc oxide nanoparticles and their antibacterial activity, *Mater. Res. Express*, 6 (2), 025016.

[58] Swaroop, K., and Somashekarappa, H.M., 2015, Effect of pH values on surface morphology and particle size variation in ZnO nanoparticles synthesised by co-precipitation method, *Res. J. Recent Sci.*, 4 (ISC-2014), 197–201.

[59] Shi, R., Yang, P., Wang, J., Zhang, A., Zhu, Y., Cao, Y., and Ma, Q., 2012, Growth of flower-like ZnO via surfactant-free hydrothermal synthesis on ITO substrate at low temperature, *CrystEngComm*, 14 (18), 5996–6003.

[60] Sounart, T.L., Liu, J., Voigt, J.A., Huo, M., Spoerke, E.D., and McKenzie, B., 2007, Secondary nucleation and growth of ZnO, *J. Am. Chem. Soc.*, 129 (51), 15786–15793.

[61] Malik, P., Shankar, R., Malik, V., Sharma, N., and Mukherjee, T.K., 2014, Green chemistry based benign routes for nanoparticle synthesis, *J. Nanopart.*, 2014, 302429.

[62] Kalimuthu, V., and Rath, S., 2015, UV photoluminescence from nanocrystalline tin oxide synthesized by a one-step hydrothermal method, *Mater. Lett.*, 157, 11–14.

[63] Gusatti, M., Campos, C.E.M., Souza, D.A.R., Moser, V.M., Kuhnen, N.C., and Riella, H.G., 2013, Effect of reaction parameters on the formation and properties of ZnO nanocrystals synthesized via a rapid solochemical processing, *J. Nanosci. Nanotechnol.*, 13 (12), 8307–8314.

[64] Aneesh, P.M., Vanaja, K.A., and Jayaraj, M.K., 2007, Synthesis of ZnO nanoparticles by hydrothermal method, *Proc. SPIE*, 6639, 66390J1.

[65] Taghizadeh, S.M., Lal, N., Ebrahiminezhad, A., Moeini, F., Seifan, M., Ghasemi, Y., and Berenjian, A., 2020, Green and economic fabrication of zinc oxide (ZnO) nanorods as a broadband UV blocker and antimicrobial agent, *Nanomaterials*, 10 (3), 530.

[66] Kaningini, A.G., Azizi, S., Sintwa, N., Mokalane, K., Mohale, K.C., Mudau, F.N., and Maaza, M., 2022, Effect of optimized precursor concentration, temperature, and doping on optical properties of ZnO nanoparticles synthesized via a green route using bush tea (*Athrixia phylicoides* DC.) leaf extracts, *ACS Omega*, 7 (36), 31658–31666.

[67] Hassan, M.M., Khan, W., Azam, A., and Naqvi, A.H., 2014, Effect of size reduction on structural and optical properties of ZnO matrix due to successive doping of Fe ions, *J. Lumin.*, 145, 160–166.

[68] Gan, F., Wu, K., Ma, F., and Du, C., 2020, In Situ Determination of nitrate in water using Fourier transform mid-infrared attenuated total reflectance spectroscopy coupled with deconvolution algorithm, *Molecules*, 25 (24), 5838.

[69] Samanta, P.K., and Bandyopadhyay, A.K., 2012, Chemical growth of hexagonal zinc oxide nanorods and their optical properties, *Appl. Nanosci.*, 2 (2), 111–117.

[70] Meddouri, M., Hammiche, L., Djouadi, D., Chelouche, A., Touam, T., and Boudine, B., 2016, Synthesis of ZnO aerogels nanopowders in supercritical methanol: Effect of sol concentration on structural, morphological and optical properties, *J. Sol-Gel Sci. Technol.*, 80 (3), 642–650.

[71] Bundit, O., and Wongsaprom, K., 2018, Shape control in zinc oxide nanostructures by precipitation method, *J. Phys.: Conf. Ser.*, 1144 (1), 012044.

[72] Costa, S.M., Ferreira, D.P., Ferreira, A., Vaz, F., and Fangueiro, R., 2018, Multifunctional flax fibres

based on the combined effect of silver and zinc oxide (Ag/ZnO) nanostructures, *Nanomaterials*, 8 (12), 1069.

[73] Nava, O.J., Soto-Robles, C.A., Gómez-Gutiérrez, C.M., Vilchis-Nestor, A.R., Castro-Beltrán, A., Olivas, A., and Luque, P.A., 2017, Fruit peel extract mediated green synthesis of zinc oxide nanoparticles, *J. Mol. Struct.*, 1147, 1–6.

[74] Gu, Y., Kuskovsky, I.L., Yin, M., O'Brien, S., and Neumark, G.F., 2004, Quantum confinement in ZnO nanorods, *Appl. Phys. Lett.*, 85 (17), 3833–3835.
Köseoğlu, Y., 2014, A simple microwave-assisted combustion synthesis and structural, optical and magnetic characterization of ZnO nanoplatelets, *Ceram. Int.*, 40 (3), 4673–4679.

[75] Basnet, P., Inakhunbi, C.T., Samanta, D., and Chatterjee, S., 2018, A review on bio-synthesized zinc oxide nanoparticles using plant extracts as reductants and stabilizing agents, *J. Photochem. Photobiol., B,* 183, 201–221.

[76] Aiempanakit, M., Sudjai, P., Singsumphan, K., Laksee, S., and Suwanchawalit, C., 2022, Brazilein modified zinc oxide nanorods with enhanced visible light-responsive photocatalytic efficiency, *J. Met., Mater. Miner.*, 32 (2), 70–76.

[77] Fatimah, I., Purwiandono, G., Citradewi, P.W., Sagadevan, S., Oh, W.C., and Doong, R., 2021, Influencing factors in the synthesis of photoactive nanocomposites of ZnO/SiO_2-porous heterostructures from montmorillonite and the study for methyl violet photodegradation, *Nanomaterials*, 11 (12), 3427.